Thermal induced spin-polarized current protected by spin-momentum locking in $ZrTe_5$ nanowires

Jiai Ning,[1] Wanli Peng,[1] Wei Wang,[2] Zhendong Chen,[1] Pei Yang,[1] Yequan Chen,[1] Yafei Zhao,[1] Yizhe Sun,[1] Moorthi Kanagaraj,[1] Long Yang,[1] Qinwu Gao,[1] Junran Zhang,[1] Degang Zhao,[3] Danfeng Pan,[1,4] Xuezhong Ruan,[1] Yao Li,[1] Wenqing Liu,[1,5] Liang He,[1,*] Zhi-Gang Chen,[6,†] and Yongbing Xu[1,7,‡]

[1]*School of Electronic Science and Engineering, Nanjing University, Nanjing 210023, China*
[2]*School of Physical and Mathematical Sciences, Nanjing Tech University, Nanjing 211816, China*
[3]*School of Materials Science and Engineering, University of Jinan, Jinan 250022, China*
[4]*Microfabrication and Integration Technology Center, Nanjing University, Nanjing 210023, China*
[5]*Department of Electronic Engineering, Royal Holloway University of London, Egham, Surrey TW200EX, United Kingdom*
[6]*Centre for Future Materials, The University of Southern Queensland, Springfield Central, Queensland 4300, Australia*
[7]*Nanjing-York Joint Center of Spintronics and NanoEngineering, and Department of Electronic Engineering, University of York, York YO105DD, United Kingdom*

(Received 5 April 2021; revised 7 June 2021; accepted 2 July 2021; published 26 July 2021)

Spin-momentum locking arising from strong spin-orbit coupling is one of the key natures of topological materials. Since charge can induce a spin polarization due to spin-momentum locking, the search for materials that exhibit this feature has become one of the top priorities in the field of spintronics. In this paper, we report the electrical detection of the spin-transport properties of $ZrTe_5$ nanowires, using a nonlocal geometry measurement. A clear hysteresis voltage signal, which depends on the relative orientations between the magnetization of the ferromagnetic electrodes and the carrier spin polarization, has been observed. The hysteresis voltage states can be reversed by altering the electron movement direction, providing direct evidence of the spin-momentum locking feature of $ZrTe_5$ nanowires and revealing its topological nature. Furthermore, the current-dependent measurement suggests that the charge (spin) current is induced by thermal effect, which utilizes the thermoelectric properties of $ZrTe_5$. Using the thermal effect to control the spin-polarized current protected by spin-momentum locking offers possibilities for small-sized devices based on the topological materials.

DOI: 10.1103/PhysRevB.104.035429

I. INTRODUCTION

One of the key characteristics of topological materials is spin-momentum locking, which is caused by a strong spin-orbit coupling. The spin-momentum locking feature has been observed in the three-dimensional topological insulators [1–4], as well as the topological Dirac-Weyl semimetals [5], following theoretical predictions [6–9]. This remarkable property leads to a charge-induced spin polarization [2,10], which can be used to enhance the spin-torque effect [5], as well as the spin Seebeck effect [11]. Therefore, topological materials with these helical surface states have great potential for applications in electronic and spintronic devices. The electrical detection of spin-polarized current protected by spin-momentum locking has become one of the top priorities in the field of spintronics.

On the other hand, with the emergence of thermospintronics (also called spin caloritronics), which refer to the manipulation of electron spins with thermal effects, the interaction between heat transport and the charge, as well as the spin degrees of freedom, has recently drawn considerable attention [12–14]. Indeed, thermoelectric effects [15,16] have demonstrated important roles in the applications of nanoelectronics, as well as spintronics [17,18]. Up to now, studies on the spin-caloritronics mostly utilize the spin freedom of ferromagnetic materials [12,13,15,19–24]. The explorations on the interplay between the thermoelectrical effect and the spin transport of topological materials are rare. Therefore, a deep understanding, as well as a utilization of the thermal effect, in spin transport based on topological materials is essential for the development of spintronics devices.

As a topological material, $ZrTe_5$ is an idea platform to investigate this interplay due to its nontrivial helical surface state, as well as strong thermoelectrical effect with a large Seebeck coefficient. Transition metal pentatelluride $ZrTe_5$ has been intensively studied due to its potential applications in thermoelectricity [25–27]. In recent years, following the discovery of topological quantum materials, $ZrTe_5$ has ignited renewed interests as a topological material [28–38]. Many intriguing properties associated with its nontrivial topological phase have been observed, such as chiral magnetic effect [29], Zeeman splitting [34–36], as well as quantum oscillations [30,31,39].

In this paper, we have carried out a systemic spin-transport measurement of $ZrTe_5$ nanowires using nonlocal

*heliang@nju.edu.cn
†zhigang.chen@usq.edu.au
‡ybxu@nju.edu.cn

geometry. The nonlocal voltage signal demonstrates a hysteresis loop as the external magnetic fields sweep back and forth. A high (low) voltage state is observed when the magnetization **M** of the ferromagnetic electrode (Py) is parallel (antiparallel) to the spin polarization **s** of the carriers. This hysteresis voltage state was reversed by altering the direction of the electron movements, which unambiguously reveals the spin-momentum locking feature of $ZrTe_5$. More importantly, the charge (spin) flow is generated and controlled by thermal effects under nonlocal geometry, and therefore, we validate a feasible method using basic thermoelectrical effect to control the charge (spin) flow in a $ZrTe_5$ nanowire.

II. EXPERIMENTAL DETAILS

A. Crystal growth

$ZrTe_5$ crystals consisting of Zr powder (purity: 99.99%) and Te powder (purity: 99.999%) were prepared via the chemical vapor transport method using iodine as the transport agent. A typical temperature gradient from 500 to 400 °C was employed. The structural characterization of obtained bulk $ZrTe_5$ crystals can be found in Fig. S1 in the Supplemental Material [40].

B. Device fabrication

The $ZrTe_5$ nanowires were exfoliated from bulk crystals, then transferred onto a precleaned SiO_2/Si substrate (t_{SiO2} = 280 nm). The contacts of the devices were patterned via standard ultraviolet exposure technology. Here, MgO (2 nm), Py (150 nm), and Au (8 nm) were deposited sequentially by electron beam evaporation. The vacuum pressure was maintained at 2×10^{-7} mbar during the deposition. The inserted thin MgO layer was used to decouple the magnetization of the Py electrodes and the $ZrTe_5$ nanowire channel. An 8 nm Au coating on the Py electrodes was used to prevent subsequent oxidation. To reduce the contamination and damage during device fabrication, four ferromagnetic contacts were used, in which the two outer Py contacts were well separated from the inner contacts. The detailed information of the contact separation can be found in Fig. S2 in the Supplemental Material [40]. This measurement geometry has been used in previous studies [41,42]. The exfoliated $ZrTe_5$ nanowires were measured by scanning electron microscope (SEM) and atomic force microscope (AFM) to determine its feature size.

C. Transport measurements

The low-temperature spin-transport measurements were performed using an Oxford instruments cryogenic system (TeslatronPT, Oxford) which can provide a magnetic field up to 14 T and temperatures down to 1.6 K. A Keithley 6221 ac/dc current source was used to apply the current, while a lock-in amplifier (Stanford Research SR830) was employed to detect the voltage signal. A lock-in technique was used to extract the relatively small spin signal from the background noise, and nonlocal measurement geometry was adopted to exclude the contact resistance and any spurious signals induced by the Py contact.

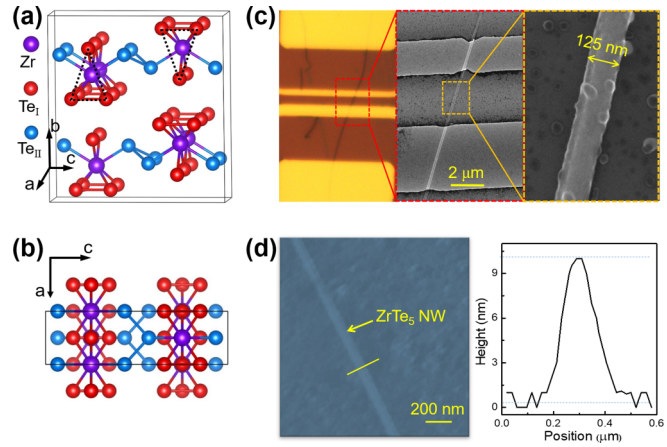

FIG. 1. Structure and morphology of $ZrTe_5$ crystal. (a) The crystal structure of $ZrTe_5$. The purple spheres represent the Zr atoms, while the red and blue spheres represent the Te atoms. The trigonal prismatic chains of $ZrTe_3$ (Te_I) run along the *a* axis (indicated by the black dashed line), forming a two-dimensional (2D) sheet of $ZrTe_5$ in the *a*-*c* plane via parallel zigzag chains of 2 Te atoms (Te_{II}). The sheets of $ZrTe_5$ stacked along the *b* axis form a layered crystal structure. (b) Top view of two $ZrTe_5$ layers. The primitive cell of two prismatic chains and two zigzag chains is indicated by a black rectangle. (c) Optical and electronic microscopic images of the device, clearly indicating four ferromagnetic (Py) contacts and the $ZrTe_5$ nanowire with a width of 125 nm. (d) Atomic force microscopy (AFM) image of the $ZrTe_5$ nanowire, from which the thickness of the nanowire is determined to be ∼10 nm.

III. RESULTS AND DISCUSSION

A. Basic characterizations

$ZrTe_5$ has a typical orthorhombic layered structure with a space group of *Cmcm* (D_{2h}^{17}) [43]. Figure 1(a) displays the schematic crystal structure of $ZrTe_5$, where the purple spheres represent the Zr atoms, and the red and blue spheres represent the prismatic (Te_I) and the zigzag (Te_{II}) Te atoms, respectively. The trigonal prismatic chains of $ZrTe_3$ (Te_I) are visible along the *a* axis (indicated by the black dashed triangle), which form a two-dimensional sheet of $ZrTe_5$ in the *a*-*c* plane via parallel zigzag chains of two Te atoms (Te_{II}). The sheet stacks along the *b* axis, coupled via weak van der Waals forces, forming a layered crystal structure. Figure 1(b) is a top view image of two $ZrTe_5$ layers, in which the primitive cell with two prismatic chains and two zigzag chains is indicated by a black dashed rectangle.

The nanowires were exfoliated along the *a*-*c* plane from bulk crystals. The developed device was inspected by SEM, and the result is shown in Fig. 1(c), from which, the width of the $ZrTe_5$ nanowire is determined to be ∼125 nm, and the thickness of the nanowire is ∼10 nm, as examined by AFM [Fig. 1(d)].

B. Theoretical understanding of the spin signal detection

In terms of the spin generation and detection under nonlocal measurement geometry, $ZrTe_5$ is well known as a

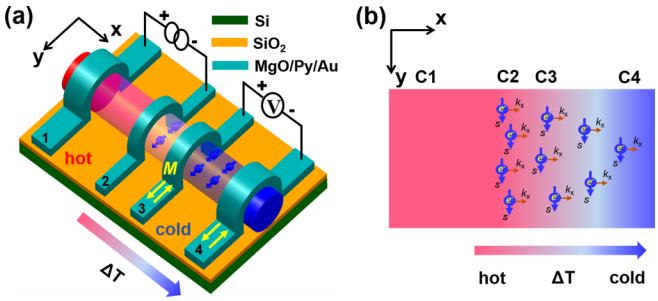

FIG. 2. Theoretical understanding of spin detection under a nonlocal geometry measurement. (a) Schematic illustration of the device structure with four ferromagnetic (Py) contacts. The currents were applied through C1 and C2, while a nonlocal voltage was measured between C3 and C4. The magnetization **M** of Py electrodes along the $+y$ or the $-y$ direction (yellow arrow) was controlled by an external magnetic field. A temperature gradient between the hot region C2 and the cold region C4 is generated by the Joule heating. (b) Schematic diagram of the migration of carriers driven by the temperature gradient. The temperature gradient defined as ΔT results in a movement of electrons from the hot region (C2) to the cold region (C4). The direction of spin polarization is indicated by the blue arrow.

thermoelectric material even at low temperatures [26,27]. This is attributed to its large thermopower P ($P = \alpha^2\sigma$) and high Seebeck coefficient $\alpha(\alpha = \Delta V/\Delta T)$, the latter of which can result in the production of a large voltage, given a small temperature gradient [44]. A schematic illustration of the device structure with four ferromagnetic (Py) contacts is shown in Fig. 2(a). When currents are applied through contact 1 (C1) and contact 2 (C2), Joule heating can be generated by the currents, and a temperature gradient is formed [45,46] between contact 2 (C2) and contact 4 (C4). The temperature gradient then drives the electrons in the $ZrTe_5$ nanowire moving along the $+x$ direction ($\mathbf{k}_x > 0$) from the high-temperature end (C2) to the low-temperature end (C4). Due to the spin-momentum locking, the right moving electrons ($\mathbf{k}_x > 0$) have a spin polarization **s** pointing along the $+y$ direction [2,3,47], as shown in Fig. 2(b).

Meanwhile, a magnetic field is sweeping back and forth to control the magnetization **M** of the Py electrode in the $+y$ or $-y$ direction indicated by the yellow arrows (defined as positive $+\mathbf{M}$ or negative $-\mathbf{M}$ magnetization, corresponding to the majority spin direction along $+y$ or $-y$ direction, respectively). Thus, the relative orientation between **M** and **s** should demonstrate parallel or antiparallel state under a sweeping field. Those states can be picked up between C3 and C4 as a high-voltage (**s**//**M**) state or a low-voltage (**s**//$-$**M**) state. Similarly, when currents are applied between contact 3 (C3) and contact 4 (C4) (Fig. S3 in the Supplemental Material [40]), a temperature gradient with the high-temperature end (C3) and the low-temperature end (C1) is formed. In this case, the carries between C3 and C1 are driven toward the $-x$ direction ($\mathbf{k}_x < 0$). Those left moving electrons ($\mathbf{k}_x < 0$) have a spin polarization **s** pointing toward the $-y$ direction due to the spin-momentum locking (Fig. S3 in the Supplemental Material [40]). Therefore, the reversed **s** should lead to reversed high-voltage (resistance) and low-voltage (resistance) states.

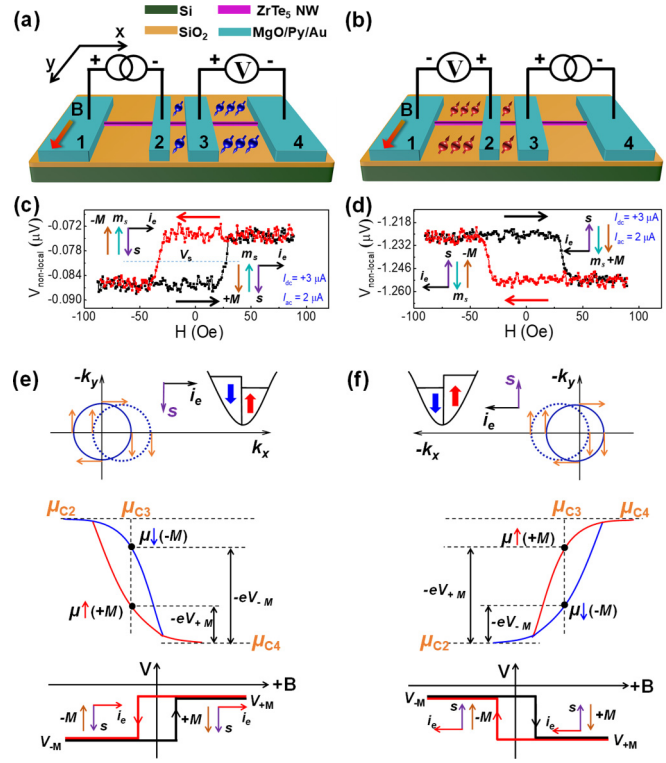

FIG. 3. Electrical detection under a nonlocal geometry setup. (a) and (b) Schematic illustration of the nonlocal geometry under a direct current (DC) bias of $I_{dc} = +3\,\mu$A and a constant alternating current (AC) of $I_{ac} = 2\,\mu$A. (a) C1 and C2 were used to applied current while the nonlocal voltage was measured between C3 and C4. (b) C3 and C4 were used to applied current while the nonlocal voltage was measured between C2 and C1. (c) and (d) The nonlocal hysteresis voltage signals at $T = 1.6$ K while the external field is sweeping back and forth. The red and black arrows indicate the magnetic field sweeping direction. The insets demonstrate that the high- or the low-voltage state is determined by the parallel or antiparallel orientation between the magnetization **M** of Py and the spin polarization **s** of the electrons. The spin polarization **s** is antiparallel to its magnetic moment $\mathbf{m}_s$ due to the negative charge of electrons. (e) and (f) Schematic diagram for the theoretical model of the spin electrochemical potential detection.

C. Electrical measurement with nonlocal geometry

Figures 3(a) and 3(b) show nonlocal measurement geometry, which is used to separate the current and the voltage circuits. In Fig. 3(a), a constant alternating current (AC) of $I_{ac} = 2\,\mu$A and a positive direct current (DC) bias of $I_{dc} = +3\,\mu$A were applied between C1 and C2 while the nonlocal voltage was picked up between C3 and C4.

As expected, both high- and low-voltage states were observed as the external magnetic field was sweeping back and forth, which is shown in Fig. 3(c). Under a large positive magnetic field, the magnetization **M** of the Py contact (C3) was along the $+y$ direction ($+\mathbf{M}$), the same as the spin polarization **s**. For clarity, it is necessary to note that the magnetic moment ($\mathbf{m}_s$) of an electron is antiparallel to its spin polarization **s** because of its negative charge [48]. Here, **M** was parallel to **s** (hence, **M** was antiparallel to $\mathbf{m}_s$), resulting in a high-voltage state, as shown by the red trace of Fig. 3(c). The high state

was maintained until the in-plane magnetic field decreased to a critical field (∼−30 Oe), which was the coercivity field of C3 (Fig. S4 in the Supplemental Material [40]). As shown in Fig. S5 in the Supplemental Material [40], this switching field decreases with the increase of temperature, which may be related to the reduced coercivity field of the Py contacts under thermal activation and suggests that the spin signals are indeed associated with the switching of the magnetization of Py. After that, the **M** was switched to the $-y$ direction ($-\mathbf{M}$), resulting in the antiparallel state between **M** and **s** (hence, **M** is parallel to $\mathbf{m}_s$). This magnetization switching led to the abrupt change from the high- to a low-voltage state [red trace of Fig. 3(c)]. A similar abrupt switch from a low- to a high-voltage state was also observed at the positive coercive field of C3 (∼30 Oe), when the magnetic field was sweeping from negative to positive, which is shown by the black trace of Fig. 3(c).

Oppositely, when the currents were applied between C3 and C4 as the nonlocal voltage signal was picked up between C1 and C2 [Fig. 3(b)], the movement of the electrons was along the $-x$ direction ($\mathbf{k}_x < 0$). In this case, a reversed hysteresis loop was observed, as displayed in Fig. 3(d), illustrating that the direction of **s** is reversed, which is caused by the opposite moving electrons. Consistent with the theoretical analysis mentioned above, those transport results demonstrate that the right moving electron ($\mathbf{k}_x > 0$) has a **s** along the $+y$ direction, while the left-moving electron ($\mathbf{k}_x < 0$) has a **s** along the $-y$ direction, providing unambiguous evidence for the spin-momentum locking feature of $ZrTe_5$ nanowires. This feature has been further confirmed by local measurement geometry (Fig. S6 in the Supplemental Material [40]).

Meanwhile, a control experiment has been carried out (Fig. S7 in the Supplemental Material [40]), in which the $ZrTe_5$ nanowire was replaced by a gold nanowire. In this case, no hysteresis signal was observed, indicating the hysteresis signals are correlated with the $ZrTe_5$ nanowire, which further rules out the effects such as anisotropic magnetoresistance (AMR) and the anomalous Hall effect (AHE), which could be induced by the Py electrodes [49,50].

To further understand the spin potentiometric, i.e., the spin-dependent voltage detected by the nonlocal measurement, Figs. 3(e) and 3(f) schematically illustrate the spin-dependent electrochemical potential (μ). Here, we take Fig. 3(e) as an example. When currents are applied through C1 and C2, the carrier momentum driven by the formed temperature gradient is along the $\mathbf{k}_x$ direction (represented by a displacement of the cross-section of the dotted blue circle along $\mathbf{k}_x$), which results in an electron current i_e along the $+x$ direction. The spin tangential at all points is shown by the solid orange arrows [shown in the top part of Fig. 3(e)]. When the magnetic field was sweeping from positive to negative, the measured voltage between C3 and C4 can be defined as V_{+M} and V_{-M}. Since the scattering is smaller as **M** and **s** are antiparallel ($\mathbf{m}_s$ parallel to **M**), i.e., when a positive magnetic field ($+B$, $+\mathbf{M}$) is applied, the Py electrode will mainly measure the electrochemical potential of spin up, not otherwise. Thus, $V_{+M} = (\mu_3 \uparrow - \mu_4)/(-e)$, and the same is $V_{-M} = (\mu_3 \downarrow - \mu_4)/(-e)$, in which $\uparrow$ and $\downarrow$ represent the s is along the $-y$ (spin up) and $+y$ (spin down) directions, respectively. Here, μ_4 can be treated as zero since it is far from C2 and C3.

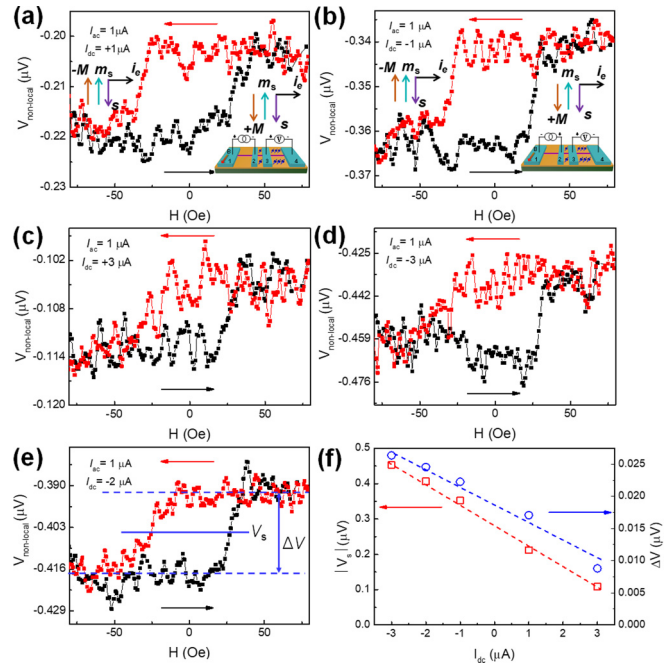

FIG. 4. Current dependent measurement. (a)–(e) Nonlocal voltage signals at 1.6 K under various direct current (DC) bias and a constant alternating current (AC) of $I_{ac} = 1\,\mu$A. (f) The absolute value of baseline voltage V_s and the spin voltage amplitude ΔV as a function of I_{dc}. A linear dependence of I_{dc} can be observed. Insets are the measurement structure.

Due to the spin-momentum locking, the electrons moving toward the $+x(\mathbf{k}_x > 0, \mathbf{s}// + \mathbf{y})$ have a higher occupation and a higher electrochemical potential (μ) than those moving to the $-x(\mathbf{k}_x < 0, \mathbf{s}// - \mathbf{y})$, as indicated by the blue and red lines in the middle of Fig. 3(e). Since $\mu\downarrow > \mu\uparrow$, V_{+M} is higher than V_{-M}, i.e., $(V_{+M} - V_{-M}) > 0$. The difference in electrochemical potentials between spin up and spin down gives rise to a voltage difference. As a direct result, the measured nonlocal voltage demonstrates a hysteresis signal with a high state under positive fields and a low state under negative fields, as shown at the bottom of Fig. 3(e). For the reversed hysteresis voltage signal shown in Fig. 3(f), it was attributed to a reversed spin polarization arising from the opposite diffused electrons, and μ_1 was treated as zero instead of μ_4.

To further confirm that the origin of the measured voltage signal is related to the thermal effect, various DC bias (from -3 μA to $+3$ μA) have been applied, and the results are shown in Fig. 4. The baseline voltage (V_s), which is in fact the Seebeck voltage, as well as the difference between the high- and the low-voltage states (ΔV), demonstrates a linear dependence on the I_{dc} bias, as shown in Fig. 4(f). Those can be understood as the following.

The measured signals are thermally induced, so they should be proportional to the heating generated at the contact C2, i.e., $\Delta T \propto Q$. [11,15,51,52]. The heating includes two parts; one is the Joule heating (Q_J):

$$\begin{aligned} Q_J \propto [I_{dc} + I_{ac}]^2 R &= [I_{dc} + I_0 \sin(\omega t)]^2 R \\ &= I_{dc}^2 + \tfrac{1}{2} I_0^2 + 2 I_{dc} I_0 \sin(\omega t) \\ &\quad - \tfrac{1}{2} I_0^2 \cos(2\omega t), \end{aligned} \tag{1}$$

where I_0 and ω are the amplitude and the frequency of the AC, respectively. The other is the Peltier heating (Q_P):

$$Q_P \propto [I_{dc} + I_{ac}]\Pi = I_{dc}\Pi + I_0 \sin(\omega t)\Pi, \quad (2)$$

where the Π is the Peltier coefficient [14]. Since we have adopted a lock-in technique to extract the voltage signal using the first harmonic response with the fundamental frequency ω, the measured signals are the components with $\sin(\omega t)$ in Eqs. (1) and (2). Thus, the voltage reading can be represented as

$$V_{nonlocal} \propto 2I_{dc}I_0 + I_0\Pi. \quad (3)$$

Therefore, under a constant AC (I_0), $V_{nonlocal}$ should have a linear dependence on I_{dc}. The nonzero intercept of $I_0\Pi$ when $I_{dc} = 0$ can be attributed to the Peltier heating, which agrees well in Fig. 4(f). Clearly, the current-dependent measurement demonstrates that the measured voltage signals are proportional to the applied DC, as expected for a thermally driven spin-transport phenomenon.

The measured nonlocal voltage signals arise from a polarized charge flow, induced by the thermal effect and protected by the spin-momentum locking, not from the diffusion of the spin accumulation, formed by the spin-polarized electrons, which are injected from the Py electrode into the $ZrTe_5$ nanowire. It is well known that the voltage arising from a spin accumulation is bipolar, having equal magnitude but opposite sign for the parallel and antiparallel alignment of both ferromagnets [53]. If there is a nonequilibrium spin accumulation, the parallel and antiparallel states should have a dependence of the applied current direction [20], which is in contrast with our observations (Fig. 4). Furthermore, the linear dependence of I_{dc} shown in Fig. 4(f) unequivocally rules out the spin diffusion, as well as the charge current spreading [54], as a main source of the spin signal (see Supplemental Material [40]).

Different from the generally used local geometry measurement [2,5,11], nonlocal geometry was used in this paper. Since the current and voltage paths are completely separated by nonlocal geometry, the spurious signals including the AMR and AHE induced by the Py electrodes are eliminated. Our transport results demonstrate that the value of $\Delta R/R_s$ (2–15%) for the nonlocal measurement (Figs. 3 and 4) is much larger than that (∼0.06%) obtained from the local measurement (Fig. S6 in the Supplemental Material [40]), suggesting that the nonlocal measurement is more suitable for spin detection.

IV. CONCLUSIONS

In summary, the spin-momentum locking feature of a $ZrTe_5$ nanowire has been successfully detected using nonlocal geometry. The control of a spin-polarized current via thermal effect is achieved, which offers possibilities for small-sized devices based on topological materials. The transport results give a physical understanding of the creation and detection of the nonlocal spin signals, in which both the topological properties and thermoelectric effects of $ZrTe_5$ have played important roles. The spin-momentum locking feature and the significant thermoelectrical properties as demonstrated in this paper can potentially be utilized to enhance the spin-torque effect of a $ZrTe_5$ nanowire, which is relevant for future magnetic-field-free spintronic devices. Even further work using a gate to control the spin transport of $ZrTe_5$ nanowires would be intriguing and promising for the topological-based spintronics devices.

ACKNOWLEDGMENTS

This paper is supported by the National Key R&D Program of China (Grants No. 2016YFA0300803 and No. 2017YFA0206304), the National Basic Research Program of China (Grant No. 2014CB921101), the National Natural Science Foundation of China (Grants No. 61674079, No. 61974061), Jiangsu NSF (Grant No. BK20140054), UK EPSRC (Grant No. EP/S010246/1), Royal Society (Grant No. IEC\NSFC\181680), and the Leverhulme Trust (Grant No. LTSRF1819\15\12).

[1] D. Hsieh, Y. Xia, D. Qian, L. Wray, J. H. Dil, F. Meier, J. Osterwalder, L. Patthey, J. G. Checkelsky, N. P. Ong, A. V. Fedorov, H. Lin, A. Bansil, D. Grauer, Y. S. Hor, R. J. Cava, and M. Z. Hasan, A tunable topological insulator in the spin helical Dirac transport regime, Nature **460**, 1101 (2009).

[2] C. H. Li, O. M. J. van 't Erve, J. T. Robinson, Y. Liu, L. Li, and B. T. Jonker, Electrical detection of charge-current-induced spin polarization due to spin-momentum locking in Bi_2Se_3, Nat. Nanotechnol. **9**, 218 (2014).

[3] J. Tang, L.-T. Chang, X. Kou, K. Murata, E. S. Choi, M. Lang, Y. Fan, Y. Jiang, M. Montazeri, W. Jiang, Y. Wang, L. He, and K. L. Wang, Electrical detection of spin-polarized surface states conduction in $(Bi_{0.53}Sb_{0.47})_2Te_3$ topological insulator, Nano Lett. **14**, 5423 (2014).

[4] J. Tian, I. Miotkowski, S. Hong, and Y. P. Chen, Electrical injection and detection of spin-polarized currents in topological insulator Bi_2Te_2Se, Sci. Rep. **5**, 14293 (2015).

[5] P. Li, W. Wu, Y. Wen, C. Zhang, J. Zhang, S. Zhang, Z. Yu, S. A. Yang, A. Manchon, and X.-x. Zhang, Spin-momentum locking and spin-orbit torques in magnetic nano-heterojunctions composed of Weyl semimetal WTe_2, Nat. Commun. **9**, 3990 (2018).

[6] A. A. Burkov and D. G. Hawthorn, Spin and Charge Transport on the Surface of a Topological Insulator, Phys. Rev. Lett. **105**, 066802 (2010).

[7] D. Culcer, E. H. Hwang, T. D. Stanescu, and S. Das Sarma, Two-dimensional surface charge transport in topological insulators, Phys. Rev. B **82**, 155457 (2010).

[8] O. V. Yazyev, J. E. Moore, and S. G. Louie, Spin Polarization and Transport of Surface States in the Topological Insulators Bi_2Se_3 and Bi_2Te_3 from First Principles, Phys. Rev. Lett. **105**, 266806 (2010).

[9] X.-Q. Sun, S.-C. Zhang, and Z. Wang, Helical Spin Order from Topological Dirac and Weyl Semimetals, Phys. Rev. Lett. **115**, 076802 (2015).

[10] A. Q. Wang, X. G. Ye, D. P. Yu, and Z. M. Liao, Topological semimetal nanostructures: From properties to topotronics, ACS Nano **14**, 3755 (2020).

[11] Z. Jiang, C.-Z. Chang, M. R. Masir, C. Tang, Y. Xu, J. S. Moodera, A. H. MacDonald, and J. Shi, Enhanced spin Seebeck effect signal due to spin-momentum locked topological surface states, Nat. Commun. **7**, 11458 (2016).

[12] A. Slachter, F. L. Bakker, J. P. Adam, and B. J. van Wees, Thermally driven spin injection from a ferromagnet into a nonmagnetic metal, Nat. Phys. **6**, 879 (2010).

[13] J. C. Le Breton, S. Sharma, H. Saito, S. Yuasa, and R. Jansen, Thermal spin current from a ferromagnet to silicon by Seebeck spin tunnelling, Nature **475**, 82 (2011).

[14] X.-L. Shi, J. Zou, and Z.-G. Chen, Advanced thermoelectric design: from materials and structures to devices, Chem. Rev. **120**, 7399 (2020).

[15] F. L. Bakker, A. Slachter, J. P. Adam, and B. J. van Wees, Interplay of Peltier and Seebeck Effects in Nanoscale Nonlocal Spin Valves, Phys. Rev. Lett. **105**, 136601 (2010).

[16] X. Su, P. Wei, H. Li, W. Liu, Y. Yan, P. Li, C. Su, C. Xie, W. Zhao, P. Zhai, Q. Zhang, X. Tang, and C. Uher, Multi-scale microstructural thermoelectric materials: Transport behavior, non-equilibrium preparation, and applications, Adv. Mater. **29**, 1602013 (2017).

[17] F. Giazotto, T. T. Heikkilä, A. Luukanen, A. M. Savin, and J. P. Pekola, Opportunities for mesoscopics in thermometry and refrigeration: Physics and applications, Rev. Mod. Phys. **78**, 217 (2006).

[18] Y. Dubi and M. Di Ventra, Colloquium: Heat flow and thermoelectricity in atomic and molecular junctions, Rev. Mod. Phys. **83**, 131 (2011).

[19] M. Erekhinsky, F. Casanova, I. K. Schuller, and A. Sharoni, Spin-dependent Seebeck effect in non-local spin valve devices, Appl. Phys. Lett. **100**, 212401 (2012).

[20] F. Casanova, A. Sharoni, M. Erekhinsky, and I. K. Schuller, Control of spin injection by direct current in lateral spin valves, Phys. Rev. B **79**, 184415 (2009).

[21] K. Uchida, S. Takahashi, K. Harii, J. Ieda, W. Koshibae, K. Ando, S. Maekawa, and E. Saitoh, Observation of the spin Seebeck effect, Nature **455**, 778 (2008).

[22] T. Kimura, T. Sato, and Y. Otani, Temperature Evolution of Spin Relaxation in a NiFe/Cu Lateral Spin Valve, Phys. Rev. Lett. **100**, 066602 (2008).

[23] M. Hatami, G. E. Bauer, Q. Zhang, and P. J. Kelly, Thermal Spin-Transfer Torque in Magnetoelectronic Devices, Phys. Rev. Lett. **99**, 066603 (2007).

[24] L. Gravier, S. Serrano-Guisan, F. Reuse, and J. P. Ansermet, Spin-dependent Peltier effect of perpendicular currents in multilayered nanowires, Phys. Rev. B **73**, 052410 (2006).

[25] T. E. Jones, W. W. Fuller, T. J. Wieting, and F. Levy, Thermoelectric powder of $HfTe_5$ and $ZrTe_5$, Solid State Commun. **42**, 793 (1982).

[26] R. T. L. IV, T. M. Tritt, J. W. Kolis, and J. W. Kolis, Transition-metal pentatellurides as potential low-temperature thermoelectric refrigeration materials, Phys. Rev. B **60**, 13453 (1999).

[27] T. M. Tritt, N. D. Lowhorn, R. T. L. IV, A. Pope, C. R. Feger, and J. W. Kolis, Large enhancement of the resistive anomaly in the pentatelluride materials $HfTe_5$ and $ZrTe_5$ with applied magnetic field, Phys. Rev. B **60**, 7816 (1999).

[28] J. L. Zhang, C. Y. Guo, X. D. Zhu, L. Ma, G. L. Zheng, Y. Q. Wang, L. Pi, Y. Chen, H. Q. Yuan, and M. L. Tian, Disruption of the Accidental Dirac Semimetal State in $ZrTe_5$ under Hydrostatic Pressure, Phys. Rev. Lett. **118**, 206601 (2017).

[29] Q. Li, D. E. Kharzeev, C. Zhang, Y. Huang, I. Pletikosić, A. V. Fedorov, R. D. Zhong, J. A. Schneeloch, G. D. Gu, and T. Valla, Chiral magnetic effect in $ZrTe_5$, Nat. Phys. **12**, 550 (2016).

[30] X. Yuan, C. Zhang, Y. Liu, A. Narayan, C. Song, S. Shen, X. Sui, J. Xu, H. Yu, Z. An, J. Zhao, S. Sanvito, H. Yan, and F. Xiu, Observation of quasi-two-dimensional Dirac fermions in $ZrTe_5$, NPG Asia Mater. **8**, e325 (2016).

[31] G. Zheng, J. Lu, X. Zhu, W. Ning, Y. Han, H. Zhang, J. Zhang, C. Xi, J. Yang, H. Du, K. Yang, Y. Zhang, and M. Tian, Transport evidence for the three-dimensional Dirac semimetal phase in $ZrTe_5$, Phys. Rev. B **93**, 115414 (2016).

[32] Y. Jiang, Z. L. Dun, H. D. Zhou, Z. Lu, K. W. Chen, S. Moon, T. Besara, T. M. Siegrist, R. E. Baumbach, D. Smirnov, and Z. Jiang, Landau-level spectroscopy of massive Dirac fermions in single-crystalline $ZrTe_5$ thin flakes, Phys. Rev. B **96**, 041101(R) (2017).

[33] P. Li, C. H. Zhang, J. W. Zhang, Y. Wen, and X. X. Zhang, Giant planar Hall effect in Dirac semimetal $ZrTe_{5-\delta}$, Phys. Rev. B **98**, 121108(R) (2018).

[34] Y. Liu, X. Yuan, C. Zhang, Z. Jin, A. Narayan, C. Luo, Z. Chen, L. Yang, J. Zou, X. Wu, S. Sanvito, Z. Xia, L. Li, Z. Wang, and F. Xiu, Zeeman splitting and dynamical mass generation in Dirac semimetal $ZrTe_5$, Nat. Commun. **7**, 12516 (2016).

[35] G. Zheng, X. Zhu, Y. Liu, J. Lu, W. Ning, H. Zhang, W. Gao, Y. Han, J. Yang, H. Du, K. Yang, Y. Zhang, and M. Tian, Field-induced topological phase transition from a three-dimensional Weyl semimetal to a two-dimensional massive Dirac metal in $ZrTe_5$, Phys. Rev. B **96**, 121401(R) (2017).

[36] J. Wang, J. Niu, B. Yan, X. Li, R. Bi, Y. Yao, D. Yu, and X. Wu, Vanishing quantum oscillations in Dirac semimetal $ZrTe_5$, Proc. Natl. Acad. Sci. USA **115**, 9145 (2018).

[37] Y. Zhang *et al.*, Electronic evidence of temperature-induced Lifshitz transition and topological nature in $ZrTe_5$, Nat. Commun. **8**, 15512 (2017).

[38] H. Weng, X. Dai, and Z. Fang, Transition-Metal Pentatelluride $ZrTe_5$ and $HfTe_5$: A Paradigm for Large-Gap Quantum Spin Hall Insulators, Phys. Rev. X **4**, 011002 (2014).

[39] H. Wang, H. Liu, Y. Li, Y. Liu, J. Wang, J. Liu, J.-Y. Dai, Y. Wang, L. Li, J. Yan, D. Mandrus, X. C. Xie, and J. Wang, Discovery of log-periodic oscillations in ultraquantum topological materials, Sci. Adv. **4**, eaau5096 (2018).

[40] See Supplemental Material at http://link.aps.org/supplemental/10.1103/PhysRevB.104.035429 for structural characterizations, information about contact separation, theoretical understanding of spin detection, AMR measurement of the Py electrode, temperature dependence of the nonlocal spin signal, local geometry measurements, the control experiment with gold nanowire, the exclusion of suspicious signal, and the discussion on the possible gate tuning.

[41] P. Bruski, Y. Manzke, R. Farshchi, O. Brandt, J. Herfort, and M. Ramsteiner, All-electrical spin injection and detection in the Co_2FeSi/GaAs hybrid system in the local and non-local configuration, Appl. Phys. Lett. **103**, 052406 (2013).

[42] M. Gurram, S. Omar, and B. J. van Wees, Electrical spin injection, transport, and detection in graphene-hexagonal boron

nitride van der Waals heterostructures: Progress and perspectives, 2D Mater. **5**, 032004 (2018).

[43] H. Fjellvåg and A. Kjekshus, Structural properties of $ZrTe_5$ and $HfTe_5$ as seen by powder diffraction, Solid State Commun. **60**, 91 (1986).

[44] T. M. Tritt, Thermoelectrics run hot and cold, Science **272**, 1276 (1996).

[45] A. Yamaguchi, S. Nasu, H. Tanigawa, T. Ono, K. Miyake, K. Mibu, and T. Shinjo, Effect of Joule heating in current-driven domain wall motion, Appl. Phys. Lett. **86**, 012511 (2005).

[46] H. Tohmyoh, T. Imaizumi, H. Hayashi, and M. Saka, Welding of Pt nanowires by Joule heating, Scripta Mater. **57**, 953 (2007).

[47] L. X. Wang, Y. Yan, L. Zhang, Z. M. Liao, H. C. Wu, and D. P. Yu, Zeeman effect on surface electron transport in topological insulator Bi_2Se_3 nanoribbons, Nanoscale **7**, 16687 (2015).

[48] B. Odom, D. Hanneke, B. D'Urso, and G. Gabrielse, New Measurement of the Electron Magnetic Moment Using a One-Electron Quantum Cyclotron, Phys. Rev. Lett. **97**, 030801 (2006).

[49] N. Nagaosa, J. Sinova, S. Onoda, A. H. MacDonald, and N. P. Ong, Anomalous Hall effect, Rev. Mod. Phys. **82**, 1539 (2010).

[50] J. Tang, C.-Y. Wang, L.-T. Chang, Y. Fan, T. Nie, M. Chan, W. Jiang, Y.-T. Chen, H.-J. Yang, H.-Y. Tuan, L.-J. Chen, and K. L. Wang, Electrical spin injection and detection in Mn_5Ge_3/Ge/Mn_5Ge_3 nanowire transistors, Nano Lett. **13**, 4036 (2013).

[51] Y. Wang, L. Yang, X. L. Shi, X. Shi, L. Chen, M. S. Dargusch, J. Zou, and Z. G. Chen, Flexible thermoelectric materials and generators: Challenges and innovations, Adv. Mater. **31**, 1807916 (2019).

[52] W. D. Liu, L. Yang, Z. G. Chen, and J. Zou, Promising and eco-friendly Cu_2X-based thermoelectric materials: Progress and applications, Adv. Mater. **32**, 1905703 (2020).

[53] S. Zhang, S. A. Dayeh, Y. Li, S. A. Crooker, D. L. Smith, and S. T. Picraux, Electrical spin injection and detection in silicon nanowires through oxide tunnel barriers, Nano Lett. **13**, 430 (2013).

[54] A.-Q. Wang, P.-Z. Xiang, X.-G. Ye, W.-Z. Zheng, D. Yu, and Z.-M. Liao, Room-Temperature Manipulation of Spin Texture in a Dirac Semimetal, Phys. Rev. Appl. **14**, 054044 (2020).